Joint Channel Estimation and Signal Detection for AFDM Transmission with Time-Domain Pilot Arrangement

Zunqi Li, *Graduate Student Member, IEEE*, Fangqing Xiao, *Graduate Student Member, IEEE*, Minjie Tang, *Member, IEEE*, Xiaojie Fang, *Member, IEEE*, Xuejun Sha, *Member, IEEE*, Dirk T. M. Slock, *Life Fellow, IEEE* and Vincent K. N. Lau, *Fellow, IEEE*

***Abstract*—Affine Frequency Division Multiplexing (AFDM) has shown great potential in high-mobility communication scenarios. However, efficient pilot design and low-complexity receiver algorithms remain challenging. In particular, conventional subcarrier-embedded and superimposed pilot schemes often suffer from excessive guard interval overhead and interference between pilots and data symbols. To overcome these limitations, this paper introduces a novel time-domain block-type pilot structure that enables effective pilot-data separation while reducing the overhead of guard intervals. Building on a parametric bilinear model derived from a time-domain basis expansion model (BEM), we propose a joint channel estimation and signal detection framework for AFDM systems. To facilitate the implementation of this framework with high computational efficiency, we develop a low-complexity sampling-based Expectation Propagation (EP) algorithm, which leverages Dirac mixture sampling approximations to simplify the computation of intractable integrals in bilinear message passing. Through benchmark comparisons with the Genie-aided bound and other established algorithms in both channel estimation and data detection, simulation results demonstrate the effectiveness of the proposed algorithm.**

***Index Terms*—Affine frequency division multiplexing, joint channel estimation and signal detection, basis expansion model, expectation propagation, parametric bilinear inference.**

I. Introduction

As communication technologies evolve toward the next generation, the introduction of higher frequency bands [1] and high-mobility scenarios such as Unmanned Aerial Vehicle (UAV) communications, Vehicle-to-Everything (V2X), and integrated Space-Air-Ground-Underwater (SAGU) networks [2] has led to increasingly severe doubly selective channels [3]. These channels are characterized by both significant multipath propagation and Doppler shifts. Such challenging propagation conditions have exposed the limitations of conventional waveforms like Orthogonal Frequency Division Multiplexing (OFDM), which perform well in low-mobility, Sub-6 GHz environments. Consequently, the development of novel waveforms such as Orthogonal Time Frequency Space (OTFS) [4] and Affine Frequency Division Multiplexing (AFDM) [5], which support robust transmission over time-frequency selective channels, has attracted growing research interest.

A. Related work

Among the emerging waveform candidates, affine frequency division multiplexing (AFDM) has recently gained increasing attention. As a chirp-based multicarrier modulation scheme, AFDM not only provides robust error performance, but also exhibits notable advantages in embedded pilot-based channel estimation [5]. Compared to the two-dimensional guard intervals required in delay-Doppler (DD) domain modulation schemes like OTFS, AFDM requires fewer guard intervals and thus provides higher spectral efficiency [6]. Benefiting from the flexible selection of dual-chirp parameters, AFDM can adapt to channel variations by tuning the chirp parameters at the transmitter and receiver sides. As a result, AFDM exhibits strong potential for achieving full path diversity [5] and equal signal-to-interference-plus-noise ratio (SINR) transmission [7]. Beyond error performance, the adjustable and extensible chirp parameters in AFDM can be leveraged for various purposes: grouping pre-chirp signals and introducing index mapping to embed additional index information [8]; reducing the peak-to-average power ratio (PAPR) in multicarrier systems by selecting appropriate pre-chirp parameter sets based on the affine-frequency-domain signal [9]; and serving as cryptographic keys to enhance secure communication between legitimate transceivers [10]. In the context of emerging requirements for next-generation standards, AFDM shows great potential in three key areas: first, when integrated with sparse code multiple access, it supports outstanding massive connectivity in high mobility channels [11]; second, its distinctive chirp subcarrier structure enables superior performance in integrated sensing and communication [12], [13];

This work was supported in part by the National Natural Science Foundation of China (Grant U23A20278), in part by the National Key Research and Development Program of China (Grant 2022YFB2902404), in part by China Scholarship Council, in part by the Research Grants Council of Hong Kong under Project CERG (Grant 16214122), and in part by the Research Grants Council of Hong Kong under the Areas of Excellence Scheme (Grant AoE/E-601/22-R). The corresponding author is Xiaojie Fang.

Zunqi Li and Xiaojie Fang are with the School of Electronics and Information Engineering, Harbin Institute of Technology, Harbin, China, and the National Key Laboratory of Advanced Communication Networks, Shijiazhuang, China. Xuejun Sha is with the School of Electronics and Information Engineering, Harbin Institute of Technology, Harbin, China (e-mail: {lizunqi@stu., fangxiaojie@, shaxuejun@}hit.edu.cn).

Fangqing Xiao, Minjie Tang, and Dirk Slock are with the Department of Communication Systems, EURECOM, 06410 Biot, France (e-mail: {Fangqing.Xiao, Minjie.Tang, Dirk.Slock}@eurecom.fr).

Vincent K. N. Lau is with the Department of Electronic and Computer Engineering, The Hong Kong University of Science and Technology, Hong Kong (e-mail: eeknlau@ust.hk).

and third, AFDM has demonstrated robust performance in non-terrestrial network (NTN) scenarios, such as aeronautical and land-mobile satellite channels [14].

Accurate channel estimation and signal detection constitute a crucial part of practical communication systems and pose significant challenges, particularly under high-mobility conditions. To address this, [5], [15] present multiple pilot embedding algorithms in the affine frequency domain. These algorithms exploit the path resolvability of the affine-frequency-domain channel for channel estimation and introduce guard intervals to mitigate interference between pilots and data symbols. [16] proposed two low-complexity detection algorithms in the affine frequency domain, which closely approaches the performance of the minimum mean square error (MMSE) equalizer. Building on this, [7] further explored the equivalence between MMSE equalization in the time domain and the affine frequency domain, and proposed a time-domain iterative equalization scheme with low complexity. To further improve spectral efficiency, [17] introduces a superimposed pilot embedding scheme that eliminates guard intervals by overlaying high-power pilots directly onto data symbols in the affine frequency domain. However, the absence of guard intervals inevitably results in severe interference between pilots and data, necessitating multiple iterations of interference cancellation. As a result, the achievable performance is constrained by residual interference [18].

The aforementioned studies on channel estimation and signal detection in AFDM systems generally follow a loose coupled design, where the estimated channel is directly provided to the detector or used for interference cancellation. These algorithms do not fully exploit the exchange of soft information between estimation and detection stages, which can be crucial for improving overall performance in complex channel conditions. As a result, joint channel estimation and signal detection techniques have attracted increasing attention in high-mobility scenarios, particularly when the channel estimation overhead is constrained due to a limited number of pilot symbols and short guard intervals, and further improvements in receiver performance are required. Such techniques have been explored in various waveform designs, including OFDM [19], faster-than-Nyquist multicarrier signaling [20], OTFS [21], [22], and AFDM [23]. By formulating the system model as a bilinear inference problem, these approaches utilize advanced message-passing algorithms, including variational Bayesian inference [24], parametric bilinear generalized approximate message passing (PBiGAMP) [25], and parametric bilinear Gaussian belief propagation (PBiGaBP) [26], to enable data-aided channel estimation and iterative signal recovery. Nevertheless, these algorithms often suffer from high computational complexity, which becomes particularly pronounced when the number of subcarriers is large, posing practical implementation challenges.

B. Motivation and Contributions

In both the subcarrier-embedded and superimposed pilot schemes discussed above, guard interval overhead and mutual interference between pilots and data remain significant challenges. This naturally raises the question: *Can one design a pilot arrangement that introduces minimal guard intervals while still effectively separating pilots from data to prevent mutual interference?*

To explore this question and enhance the receiver performance of AFDM systems with low complexity, we investigate a novel pilot arrangement along with a joint channel estimation and signal detection framework for AFDM systems. The main contributions of this work are as follows:

- Inspired by the narrower band structure of the time-domain channel matrix compared to its affine-frequency-domain counterpart, we propose a block-type time-domain pilot arrangement to reduce channel estimation overhead. We further compare the pilot arrangement schemes in both domains and analyze their respective transmission efficiencies.
- We introduce a time-domain channel approximation based on the basis expansion model (BEM) to achieve a compact parametric representation of the AFDM time-domain received signal. Building upon this, we formulate a parametric bilinear inference problem and construct a corresponding factor graph to enable efficient inference within the JED framework.
- Leveraging the expectation propagation (EP) rule, we derive the message update rules and approximate the intractable integrals arising in the bilinear model using Dirac mixture sampling, which serve as an efficient approximation of Gaussian distribution. Based on this, we develop a sampling-based EP (SEP) algorithm for JED in AFDM systems.
- Through numerical simulations, we verify the effectiveness of the time-domain pilot arrangement and benchmark the proposed SEP algorithm against existing baselines. The SEP algorithm achieves performance close to the state-of-the-art PBiGAMP, exhibiting only a slight gap to the genie-aided bound in terms of normalized mean squared error (NMSE) and bit error rate (BER), while maintaining lower computational complexity than PBiGAMP.

C. Organization and Notation

The rest of the paper is organized as follows. Section II reviews the basic concepts of AFDM, DD channels, and the basis expansion model (BEM), which serve as the foundation for the proposed pilot arrangement and transceiver system model introduced in Section III. Section IV presents the joint channel and data estimation scheme within the SEP framework. Simulation results for the proposed algorithm are provided in Section V. Finally, conclusions are drawn in Section VI.

We use b to denote a scalar, $\mathbf{b}$ a vector, and $\mathbf{B}$ a matrix. $\mathbf{I}_N$, and $\mathbf{0}_N$ denote the $N \times N$ identity matrix and zero matrix, respectively. $(\cdot)^{\mathrm{H}}$ represents the conjugate transpose, and $(\cdot)^n$ denotes the n-th power. $\mathcal{D}(\mathbf{B})$ returns a vector composed of the diagonal elements of the matrix $\mathbf{B}$. The notation $[b]_N$ means taking the modulo operation of b with respect to N. The notation $\lfloor b \rfloor$ and $\lceil b \rceil$ means taking the floor operation

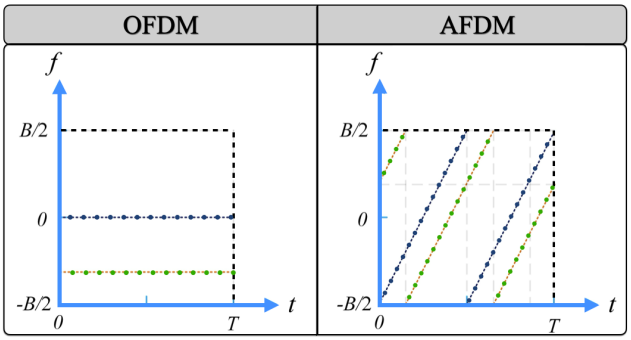

Fig. 1: The time-frequency representation of AFDM and OFDM subcarriers.

applied to the value of b. $\mathbf{B}_{(i,j)}$ represents the element in the i-th row and j-th column of matrix $\mathbf{B}$, and $\mathbf{b}_{(i)}$ represent the i-th element of vectors $\mathbf{b}$.

II. Preliminaries

In this section, we review the basic concepts of AFDM, the delay-Doppler-based channel representation, and the BEM used for channel approximation.

A. AFDM

AFDM introduces a novel approach to multicarrier modulation by employing chirp-based waveforms that spread information across both time and frequency dimensions. Unlike conventional systems such as OFDM, where each subcarrier is confined to a fixed frequency bin, AFDM modulates data using chirp-like subcarriers that evolve over time and frequency simultaneously. This structural distinction endows AFDM with superior resilience to interference and fading. Fig. 1 illustrates the distinct time-frequency representations of AFDM and OFDM subcarriers.

The core innovation of AFDM lies in its adoption of the Discrete Affine Fourier Transform (DAFT) and its inverse (IDAFT), which extend the conventional Fourier transform by incorporating two chirp parameters, c_1 and c_2. These parameters introduce controlled quadratic phase variations in both the time and frequency domains. The transmitted signal $\mathbf{s}$ in the time domain is obtained by applying the IDAFT to the data vector $\mathbf{x} \in \mathbb{C}^{N\times 1}$, as described by the following expression:

$$S_m = \frac{1}{\sqrt{N}} \sum_{n=0}^{N-1} x_n \varphi_n(m),\ m = 0, 1, \ldots, N-1, \quad (1)$$

where $\varphi_n(m) = e^{j2\pi(c_1 n^2 + \frac{1}{N}mn + c_2 m^2)}$ represents the chirp orthogonal basis functions of IDAFT, and c_1 and c_2 represent the two chirp parameters that determine IDAFT and DAFT.

Note that the expression in (1) can be written in matrix form as $\mathbf{s} = \mathbf{A}^{\mathrm{H}}\mathbf{x} \in \mathbb{C}^{N\times 1}$, where $\mathbf{A}^{\mathrm{H}} \in \mathbb{C}^{N\times N}$ is the IDAFT matrix and $\mathbf{A}$ is the DAFT matrix. The matrix $\mathbf{A}$ can be computed using the diagonal matrices $\mathbf{\Lambda_{c_1}}$ and $\mathbf{\Lambda_{c_2}}$, as well as the discrete Fourier matrix $\mathbf{F}$:

$$\mathbf{A} = \mathbf{\Lambda_{c_2}} \mathbf{F} \mathbf{\Lambda_{c_1}}, \quad (2)$$

where $\mathbf{\Lambda_c} = \mathrm{diag}(e^{-j2\pi c n^2}, n = 0, 1, \ldots, N-1) \in \mathbb{C}^{N\times N}$, and $\mathbf{F} \in \mathbb{C}^{N\times N}$ can be efficiently computed using FFT. Compared to FFT, DAFT requires $2N$ extra complex multiplication operations which results in a slight increase in complexity.

Due to the unitary property of DAFT, the IDAFT can be represented as

$$\mathbf{A}^{-1} = \mathbf{A}^{\mathrm{H}} = \mathbf{\Lambda}_{c_1}^{\mathrm{H}} \mathbf{F}^{\mathrm{H}} \mathbf{\Lambda}_{c_2}^{\mathrm{H}}. \quad (3)$$

In the AFDM receiver, the DAFT is applied to convert the time-domain signal back to the affine frequency domain, enabling further signal processing such as demodulation or equalization.

B. Channel

The channel response can be characterized using the DD representation as follows.

$$h(\tau, \nu) = \sum_{i=1}^{N_{\text{path}}} h_i \delta(\tau - \tau_i)\delta(\nu - \nu_i), \quad (4)$$

where N_{path} denotes the number of propagation paths, and h_i, τ_i, and ν_i represent the complex path gain, delay, and Doppler shift associated with the i-th path, respectively. Within the geometric coherence time, the physical propagation paths are assumed to remain time-invariant, implying that the associated delay and Doppler parameters (τ_i, ν_i) are constant over the considered time interval.

To facilitate practical implementation, the DD coordinates (τ_i, ν_i) are typically mapped to normalized delay and Doppler taps. Specifically, the corresponding delay tap l_i and Doppler tap f_i for the i-th path can be determined based on the system bandwidth B and subcarrier spacing Δf as follows:

$$\begin{aligned} l_i &= B\tau_i, \quad l_i \in [0, l_{\max}], \\ f_i &= \frac{\nu_i}{\Delta f}, \quad f_i \in [-f_{\max}, f_{\max}]. \end{aligned} \quad (5)$$

We assume that each Doppler shift follows the Jakes spectrum, i.e., $\nu_i = f_c v \cos(\theta_i)/c$, where f_c denotes the carrier frequency, v is the terminal speed, c is the speed of light, and θ_i is uniformly distributed as $\theta_i \sim \mathcal{U}[-\pi, \pi]$. For typical parameters $f_c = 6$ GHz, $v = 550$ km/h, and $\Delta f = 15$ kHz, the resulting Doppler tap satisfies $|f_i| \leq 0.2$. To accommodate higher carrier frequencies, the subcarrier spacing in 5G NR is designed as an integer multiple of 15 kHz. Moreover, in wideband systems, the time resolution is sufficiently high such that fractional delay taps can be approximated by integer values. Therefore, in the sequel, we consider doubly selective (underspread) channels characterized by integer-spaced delay taps and fractional Doppler shifts, with each Doppler tap satisfying $|f_i| < 0.5$.

For a transmission block of length N with a cyclic prefix (CP) [1], the matrix $\mathbf{H}_{\mathrm{t}} \in \mathbb{C}^{N\times N}$ can be expressed as

$$\mathbf{H}_{\mathrm{t}} = \sum_{i=1}^{N_{\text{path}}} h_i \mathbf{\Delta}_{f_i} \mathbf{\Pi}_N^{l_i}, \quad (6)$$

[1] Analogous to the CP used in OFDM, the AFDM system introduces a chirp-periodic cyclic prefix (CCP). Under the conditions that N is even and $2Nc_1 \in \mathbb{Z}$, the CCP is equivalent to the conventional CP.

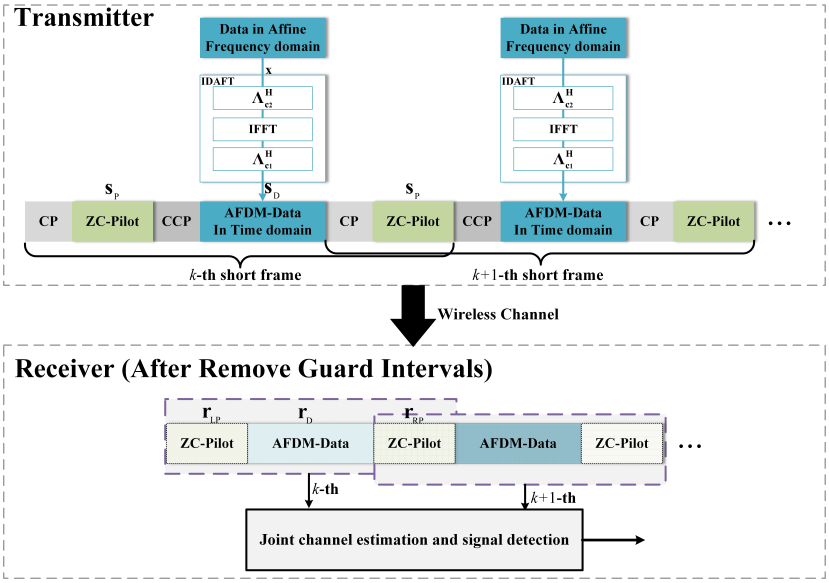

Fig. 2: AFDM baseband transmission framework with time-domain pilot arrangement.

where $\mathbf{\Delta}_{f_i} = \mathrm{diag}(e^{-j\frac{2\pi}{N}f_i n}, n = 0, 1, \ldots, N-1)$ represents the diagonal Doppler shift matrix, and $\mathbf{\Pi}_N \in \mathbb{C}^{N\times N}$ is the cyclic shift matrix, defined as:

$$\mathbf{\Pi}_N = \begin{bmatrix} 0 & \cdots & 0 & 1 \\ 1 & 0 & \cdots & 0 \\ \vdots & \ddots & \ddots & \vdots \\ 0 & \cdots & 1 & 0 \end{bmatrix}. \tag{7}$$

C. Basis expansion channel model

Both the superimposed pilot scheme [17] and the single-subcarrier pilot embedding scheme [5] are typically designed under the assumption that each delay tap is associated with a single dominant Doppler component. This idealized sparsity facilitates path-wise channel estimation and is particularly suited for open environments with well-separated scatterers. However, such models fail to capture the complexity of rich-scattering scenarios, such as V2X, where each delay tap may encompass multiple Doppler components [18], [27].

To overcome this challenge, we leverage a BEM approach that describes these overlapping paths at the same delay tap using basis functions. Specifically, the contribution of each path to the overall signal is modeled as a weighted sum of orthogonal basis functions, enabling a more compact and efficient representation of the time-varying channel characteristics.

Among various BEMs, the discrete prolate spheroidal basis expansion model (DPS-BEM) is particularly attractive due to its time-concentrated and band-limited basis functions [28]. For a given sequence length N, the DPS is defined as the eigenvectors of matrix $\mathbf{\Psi} \in \mathbb{C}^{N\times N}$, given by:

$$\mathbf{\Psi}\boldsymbol{\phi}_d = \lambda_i \boldsymbol{\phi}_d, \tag{8}$$

where the matrix elements are given by

$$\mathbf{\Psi}_{(a,b)} = \frac{\sin[2\pi(a-b)f_{\max}/N]}{\pi(a-b)}, \quad a, b \in \{1, \ldots, N\}. \tag{9}$$

The eigenvalue $\lambda_i \in [0, 1]$ quantifies the energy concentration ratio within the specified Doppler bandwidth $[-f_{\max}, f_{\max}]$. The dominant eigenvectors are typically selected for channel modeling. Therefore, the l-th delay tap corresponding path in (6) can be expressed as a weighted superposition of D dominant DPS sequences, as follows:

$$\mathbf{h}_l = \sum_{i:l_i=l} h_i \mathcal{D}(\mathbf{\Delta}_{f_i}) = \sum_{d=1}^{D} b_{l,d}\boldsymbol{\phi}_d + \epsilon_l \approx \mathbf{\Phi}\mathbf{b}_l, \tag{10}$$

where D is the basis dimension determined by $D = \lceil 2f_{\max} \rceil + 1$, $\mathbf{\Phi} \in \mathbb{C}^{N*D}$ denotes the matrix consist of basis expansion function $\boldsymbol{\phi}_d$, $\mathbf{b}_l = [b_{l,1}, \cdots, b_{l,D}]^{\mathrm{T}} \in \mathbb{C}^{D*1}$ is the corresponding coefficient and $\epsilon \in \mathbb{C}^{N*1}$ is the model error. Due to the negligible modeling error of the BEM, we omit it in subsequent analyses for the sake of analytical tractability.

III. System Model with Time-Domain Pilot Arrangement

Based on the AFDM signal and channel model presented in Section II, we propose a transmission framework with time-domain pilot arrangement and compare it with its affine-frequency-domain counterpart.

A. Tranceiver design

Fig. 2 illustrates the proposed AFDM baseband transmission framework with time-domain pilot arrangement, departing from conventional affine-frequency-domain chirp subcarrier pilot arrangements [5].

At the transmitter, Zadoff-Chu (ZC) sequence pilots and AFDM-modulated time-domain data blocks are alternately structured with guard intervals. The composite signal frame is defined as:

$$\mathbf{s}_0 = [\mathbf{s}_{\mathrm{CP}}; \mathbf{s}_{\mathrm{P}}; \mathbf{s}_{\mathrm{CCP}}; \mathbf{s}_{\mathrm{D}}; \mathbf{s}_{\mathrm{CP}}; \mathbf{s}_{\mathrm{P}}], \tag{11}$$

where the components of the composite signal frame are detailed as follows:

- ZC Pilots:

$$\mathbf{s}_{\mathrm{P}(n)} = e^{-j\pi\kappa n(n+1)/N_{\mathrm{P}}}, \quad n = 0, 1, ..., N_{\mathrm{P}} - 1, \quad (12)$$

represent identical ZC sequence pilots placed at both ends of the data block. The root index κ is coprime to the pilot length N_{P}.

- AFDM-Modulated Data:

$$\mathbf{s}_{\mathrm{D}} = \mathbf{A}^{\mathrm{H}}\mathbf{x} \in \mathbb{C}^{N_{\mathrm{D}}\times 1}, \quad (13)$$

where $\mathbf{x}$ denotes the symbol sequence generated by mapping the input bit stream onto an M-ary constellation alphabet $\mathcal{S} = \{\alpha_0, \alpha_1, \ldots, \alpha_{M-1}\}$. The vector $\mathbf{s}_{\mathrm{D}}$ represents the time-domain signal obtained by applying the inverse DAFT matrix $\mathbf{A}^{\mathrm{H}}$ to $\mathbf{x}$.

- Guard Intervals:

$$\begin{aligned}\mathbf{s}_{\mathrm{CCP}(N_{\mathrm{CP}}+n_{\mathrm{cp}})} &= \mathbf{s}_{\mathrm{D}(N_{\mathrm{D}}+n_{\mathrm{cp}})} e^{-j2\pi c_1(N_{\mathrm{D}}^2+2Nn_{\mathrm{cp}})},\\ \mathbf{s}_{\mathrm{CP}(N_{\mathrm{CP}}+n_{\mathrm{cp}})} &= \mathbf{s}_{\mathrm{P}(N_{\mathrm{P}}+n_{\mathrm{cp}})}, n_{\mathrm{cp}} = -N_{\mathrm{CP}}, \cdots, -1, \end{aligned} \quad (14)$$

represent the CCP [5] for data and the CP for pilots, respectively. To mitigate inter-block interference between pilots and data, the cyclic prefix length should satisfy $N_{\mathrm{CP}} \geq l_{\max}$.

Due to the identical pilot design, the first CP can be regarded both as the CP of $\mathbf{s}_{\mathrm{P}}$ and as the CP of the subsequent composite signal $\mathbf{s} = [\mathbf{s}_{\mathrm{P}}; \mathbf{s}_{\mathrm{CCP}}; \mathbf{s}_{\mathrm{D}}; \mathbf{s}_{\mathrm{CP}}; \mathbf{s}_{\mathrm{P}}] \in \mathbb{C}^{N\times 1}$. After removing the first CP from $\mathbf{s}_0$, the received signal corresponding to $\mathbf{s}$ passing through a doubly selective channel with additive white Gaussian noise (AWGN) can be expressed as:

$$\mathbf{r} = \mathbf{H}_t\mathbf{s} + \mathbf{n}, \quad (15)$$

where $\mathbf{r} \in \mathbb{C}^{N\times 1}$ represents the received signal, and $\mathbf{n} \in \mathbb{C}^{N\times 1}$ is complex-valued AWGN with $\mathbf{n} \sim \mathcal{CN}(\mathbf{0}, \sigma_{\mathrm{n}}^2\mathbf{I}_N)$. Assuming that the transmission duration of $\mathbf{s}_0$ does not exceed the geometric coherence time, the delay and Doppler shifts of the channel paths are considered invariant. Under this assumption, the time domain channel matrix $\mathbf{H}_t$ can be expressed as described in (6).

By further removing the guard interval between the pilot and data, the pilot and data can be considered mutually orthogonal. The subsampled received signal can then be expressed as:

$$\begin{bmatrix}\mathbf{r}_{\mathrm{LP}}\\ \mathbf{r}_{\mathrm{D}}\\ \mathbf{r}_{\mathrm{RP}}\end{bmatrix} = \begin{bmatrix}\mathbf{V}_{\mathrm{LP}}\mathbf{r}\\ \mathbf{V}_{\mathrm{D}}\mathbf{r}\\ \mathbf{V}_{\mathrm{RP}}\mathbf{r}\end{bmatrix} \triangleq \begin{bmatrix}\mathbf{H}_{\mathrm{LP}} & \mathbf{0} & \mathbf{0}\\ \mathbf{0} & \mathbf{H}_{\mathrm{D}} & \mathbf{0}\\ \mathbf{0} & \mathbf{0} & \mathbf{H}_{\mathrm{RP}}\end{bmatrix}\begin{bmatrix}\mathbf{s}_{\mathrm{P}}\\ \mathbf{s}_{\mathrm{D}}\\ \mathbf{s}_{\mathrm{P}}\end{bmatrix} + \begin{bmatrix}\mathbf{n}_{\mathrm{LP}}\\ \mathbf{n}_{\mathrm{D}}\\ \mathbf{n}_{\mathrm{RP}}\end{bmatrix}, \quad (16)$$

where

$$\begin{aligned}\mathbf{V}_{\mathrm{LP}} &= [\mathbf{I}_{N_{\mathrm{P}}}, \mathbf{0}_{N_{\mathrm{P}}*(N-N_{\mathrm{P}})}],\\ \mathbf{V}_{\mathrm{D}} &= [\mathbf{0}_{N_{\mathrm{D}}*(N_{\mathrm{P}}+N_{\mathrm{CP}})}, \mathbf{I}_{N_{\mathrm{D}}}, \mathbf{0}_{N_{\mathrm{D}}*(N_{\mathrm{P}}+N_{\mathrm{CP}})}],\\ \mathbf{V}_{\mathrm{RP}} &= [\mathbf{0}_{N_{\mathrm{P}}*(N-N_{\mathrm{P}})}, \mathbf{I}_{N_{\mathrm{P}}}],\end{aligned} \quad (17)$$

denote the corresponding subsampling matrices. Due to the properties of AWGN, time-domain subsampling does not affect the noise distribution. Therefore, the noise components of $\mathbf{n}_{\mathrm{LP}}$, $\mathbf{n}_{\mathrm{D}}$, , and $\mathbf{n}_{\mathrm{RP}}$ are assumed to follow $\mathbf{n} \sim \mathcal{CN}(\mathbf{0}, \sigma_{\mathrm{n}}^2\mathbf{I}_{N_{\mathrm{P}}})$, $\mathbf{n} \sim \mathcal{CN}(\mathbf{0}, \sigma_{\mathrm{n}}^2\mathbf{I}_{N_{\mathrm{D}}})$ and $\mathbf{n} \sim \mathcal{CN}(\mathbf{0}, \sigma_{\mathrm{n}}^2\mathbf{I}_{N_{\mathrm{P}}})$, respectively.

B. Comparison of time-domain and affine-frequency-domain pilot arrangement

Fig. 3 compares the time-domain and affine frequency-domain pilot arrangement schemes, highlighting their structural differences.

In the time-domain approach, guard intervals are inserted between adjacent blocks along the time domain, placing pilot symbols outside the data blocks to facilitate channel estimation [29], [30]. In contrast, the affine-frequency-domain arrangement distributes guard intervals across subcarriers, embedding both pilots and data symbols within the same block.

The guard intervals serve to prevent mutual interference between pilot and data symbols. Accordingly, the required guard interval lengths, denoted by Q_{t} and Q_{af}, depend on the effective bandwidths (i.e., the number of non-zero elements) of the equivalent channel matrices in the time and affine-frequency domains, respectively.

To illustrate the differences of these equivalent channels, we first recall that the time-domain equivalent channel matrix follows a similar form to that in (6), while the affine-frequency-domain counterpart is given by:

$$\mathbf{H}_{\mathrm{af}} = \sum_{i=1}^{N_{\mathrm{path}}} h_i\mathbf{H}_i = \sum_{i=1}^{N_{\mathrm{path}}} h_i\mathbf{A}\boldsymbol{\Delta}_{f_i}\boldsymbol{\Pi}_{N_{\mathrm{D}}}^{l_i}\mathbf{A}^{\mathrm{H}}, \quad (18)$$

where $\mathbf{H}_i$ corresponds to the i-th propagation path. The entries of $\mathbf{H}_i$ can be explicitly expressed as:

$$\mathbf{H}_{i(a,b)} = \frac{1}{N}e^{\frac{j2\pi}{N_{\mathrm{D}}}\left(c_1N_{\mathrm{D}}l_i^2 - bl_i + c_2N_{\mathrm{D}}(a^2-b^2)\right)}\mathbf{T}_{i(a,b)}, \quad (19)$$

where

$$\begin{aligned}\mathbf{T}_{i(a,b)} &= \sum_{n=0}^{N_{\mathrm{D}}-1} e^{-\frac{j2\pi}{N_{\mathrm{D}}}(a-b+f_i+2N_{\mathrm{D}}c_1l_i)n}\\ &= \frac{e^{-j2\pi(a-b+f_i+2N_{\mathrm{D}}c_1l_i)} - 1}{e^{-j2\pi(a-b+f_i+2N_{\mathrm{D}}c_1l_i)/N_{\mathrm{D}}} - 1}.\end{aligned} \quad (20)$$

Under a fractional Doppler shift condition where $|f_i| < 0.5$, the term $\mathbf{T}_{i(a,b)}$ is effectively non-zero only within a localized region centered at $b = [a + \mathrm{loc}_i]_{N_{\mathrm{D}}}$, spanning approximately $2k_v + 1$ entries [5]. Here, $\mathrm{loc}_i = [2Nc_1l_i]_{N_{\mathrm{D}}}$, k_v denotes a predefined sensitivity threshold introduced by the fractional Doppler shifts, and the notation $[\cdot]_{N_{\mathrm{D}}}$ represents the modulo-N_{D} operation.

For illustration, we consider a simplified example involving 16×16 equivalent channel matrices in both the time-domain and affine-frequency-domain under a two-path DD channel, as depicted in Fig. 3. In the affine-frequency-domain case (with $k_v = 2$), dark-colored regions highlight the central non-zero entries of $\mathbf{H}_i$ whereas the light-colored regions represent the energy leakage range caused by fractional Doppler shifts. As observed from the figure, the time-domain channel matrix is sparse and concentrated near the main diagonal, which reflects the limited delay spread of the channel. Consequently, the corresponding guard interval Q_{t} only needs to span this delay spread in order to suppress inter-block interference. In contrast, the affine-frequency-domain channel matrix demonstrates a broader dispersion of non-zero elements, stemming from the joint delay-Doppler effect inherent in the AFDM

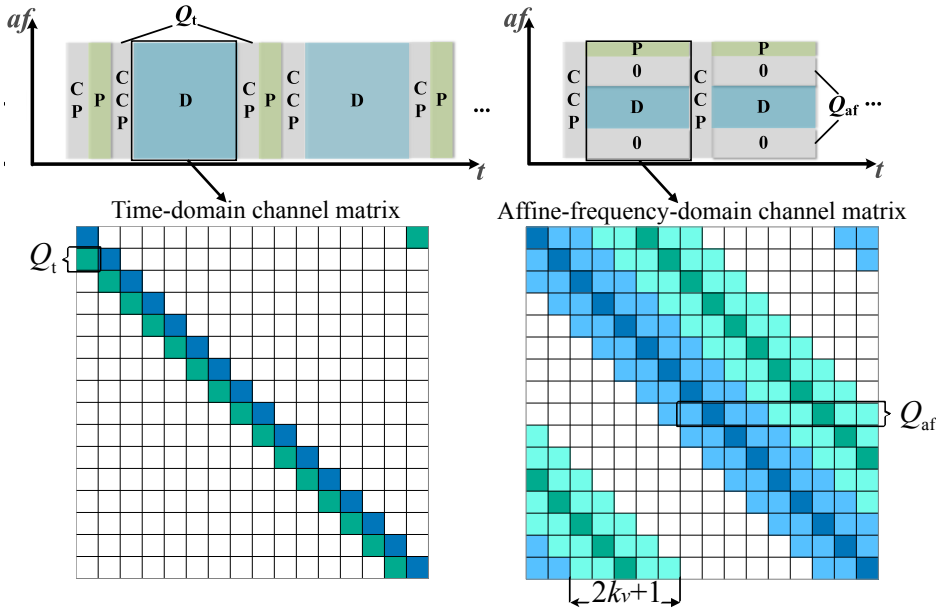

Fig. 3: Comparison of pilot arrangement schemes in the time and affine-frequency domains. ('P': pilot symbol; '0': guard interval in the affine-frequency-domain; 'D': data symbol; 'CP', 'CCP': guard intervals in the time-domain).

system. This results in a larger effective bandwidth and thus necessitates a longer guard interval Q_{af} to avoid interference between pilot and data symbols.

Moreover, due to the alternating arrangement of pilot and data blocks, every two short frames share a single pilot symbol. This design further improves spectral efficiency. As the number of consecutively transmitted short frames K increases, the spectral efficiency is further enhanced due to the amortized overhead of the pilot symbol. By jointly considering the CCP, guard intervals, and pilot overhead, we introduce the metric of transmission efficiency, defined as the ratio of the data payload length to the total transmission length. For the time-domain scheme, the transmission efficiency is given by:

$$\lambda_{\text{t}} = \frac{N_{\text{D}}}{K(N_{\text{D}} + 3Q_t + 2N_{\text{P}})} + \frac{(K-1)N_{\text{D}}}{K(N_{\text{D}} + 2Q_t + N_{\text{P}})}. \quad (21)$$

As $K \to \infty$, we have

$$\lambda_t \to \frac{N_{\text{D}}}{N_{\text{D}} + 2Q_{\text{t}} + N_{\text{P}}}. \quad (22)$$

where $Q_{\text{t}} = N_{\text{CP}} = l_{\max}$.

As a comparison, the transmission efficiency of the affine-frequency-domain scheme is given by

$$\lambda_{\text{af}} = \frac{N_{\text{D}} - 2Q_{\text{af}} - 1}{N_{\text{D}} + Q_{\text{t}}} < \frac{N_{\text{D}}}{N_{\text{D}} + Q_{\text{t}} + 2Q_{\text{af}} + 1}. \quad (23)$$

where $Q_{\text{af}} = (2k_v + 1)(l_{\max} + 1) - 1$.

Accordingly, under the large-K transmission assumption, the time-domain scheme can be approximately considered to achieve higher transmission efficiency as long as $N_{\text{P}} < (4k_v + 1)(l_{\max} + 1)$. To satisfy the condition for a non-underdetermined estimation problem, we recommend choosing the pilot length N_p such that $l_{\max}+1 \le N_p < (4k_v+1)(l_{\max}+1)$. This flexible design range enables a balanced trade-off between channel estimation accuracy and pilot overhead, and offers improved transmission efficiency over the affine-frequency-domain pilot arrangement. The effectiveness of both schemes under different transmission efficiency settings is further evaluated in the simulation section.

IV. SEP-BASED JOINT ESTIMATION AND DETECTION

Building on the transmission design introduced in the previous section, we present a joint channel estimation and data detection framework based on the time-domain BEM model, including the construction of a factor graph and the derivation of the SEP algorithm, along with a discussion of its performance and implementation aspects.

A. Parametric bilinear problem

By jointly considering the BEM in (10) and time-domain subsampling in (17), the time-domain channel matrix corresponding to the data block can be reconstructed as

$$\begin{aligned}\mathbf{H}_{\text{D}} &= \sum_{l=0}^{l_{max}} \text{diag}\left(\mathbf{V}_{\text{D}}\mathbf{h}_l\right)\mathbf{\Pi}_{N_{\text{D}}}^{l} \\ &= \sum_{l=0}^{l_{max}} \text{diag}\left(\mathbf{V}_{\text{D}}\mathbf{\Phi}\boldsymbol{b}_l\right)\mathbf{\Pi}_{N_{\text{D}}}^{l} \\ &= \sum_{l=0}^{l_{max}}\sum_{d=1}^{D} b_{l,d}\text{diag}(\mathbf{V}_{\text{D}}\boldsymbol{\phi}_d)\mathbf{\Pi}_{N_{\text{D}}}^{l} \\ &\triangleq \sum_{q=1}^{Q} b_q\mathbf{H}_q, \end{aligned} \quad (24)$$

where $\mathbf{H}_q = \text{diag}\left(\mathbf{V}_{\text{D}}\boldsymbol{\phi}_q\right)\mathbf{\Pi}_{N_{\text{D}}}^{l}$, $d = [q]_D$ and $l = \left\lfloor \frac{q}{D} \right\rfloor$.

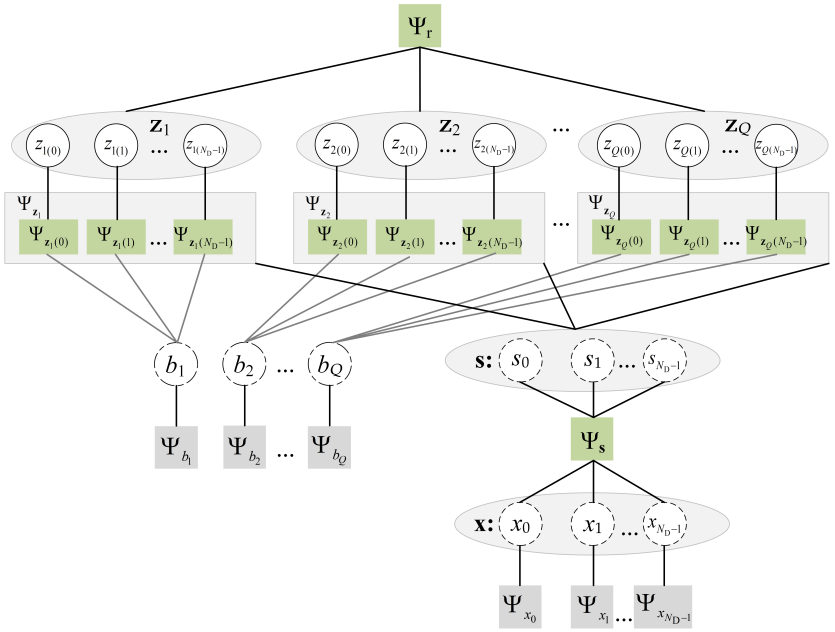

Fig. 4: Factor graph of the parametric bilinear estimation problem in (24).

Further, the observation model for $\mathbf{r}_{\mathrm{D}}$ can be expressed as

$$\mathbf{r}_{\mathrm{D}} = \sum_{q=1}^{Q} b_q \mathbf{H}_q \mathbf{s} + \mathbf{n}_{\mathrm{D}} = \sum_{q=1}^{Q} b_q \mathbf{H}_q \mathbf{A}^{\mathrm{H}} \mathbf{x} + \mathbf{n}_{\mathrm{D}}. \tag{25}$$

This formulation leads to a parametric bilinear estimation problem, where the objective is to jointly estimate the channel-related parameter $\mathbf{b} = \{b_q\}_{q=1}^{Q}$ and detect the transmitted signal $\mathbf{x}$ from the noisy observation $\mathbf{r}_{\mathrm{D}}$.

By introducing an auxiliary variable $\mathbf{z}_q = b_q \mathbf{H}_q \mathbf{A}^{\mathrm{H}} \mathbf{x}$, the joint probability density function (PDF) can be derived as

$$p(\mathbf{r}_{\mathrm{D}}, \{\mathbf{z}_q\}_{q=1}^{Q}, \mathbf{x}, \mathbf{b} \mid \mathbf{r}_{\mathrm{LP}}, \mathbf{r}_{\mathrm{RP}}) = p(\mathbf{r}_{\mathrm{D}} \mid \mathbf{z}_1, \ldots, \mathbf{z}_Q) \cdot \prod_q p(\mathbf{z}_q \mid \mathbf{s}, b_q) p(\mathbf{s} \mid \mathbf{x}) \prod_n p(x_n) \prod_q p(b_q \mid \mathbf{r}_{\mathrm{LP}}, \mathbf{r}_{\mathrm{RP}}). \tag{26}$$

The factor graph for (26) is illustrated in Fig. 4. For simplicity, the factors in the factorization (26) are denoted as

$$\Psi_{\mathbf{r}} = p(\mathbf{r}_{\mathrm{D}} \mid \mathbf{z}_1, \ldots, \mathbf{z}_Q) = \mathcal{CN}\left(\mathbf{r}_{\mathrm{D}}; \sum_q \mathbf{z}_q, \sigma_n^2 \mathbf{I}_{N_{\mathrm{D}}}\right), \tag{27a}$$

$$\Psi_{\mathbf{z}_q} = p(\mathbf{z}_q \mid \mathbf{s}, b_q) = \delta(\mathbf{z}_q - b_q \mathbf{H}_q \mathbf{s}), \tag{27b}$$

$$\Psi_{\mathbf{s}} = p(\mathbf{s} \mid \mathbf{x}) = \delta(\mathbf{s} - \mathbf{A}^{\mathrm{H}} \mathbf{x}), \tag{27c}$$

$$\Psi_{x_n} = p(x_n) = \sum_{\alpha_i \in \Omega} P(\mathbf{x}_n = \alpha_i) \delta(x_n - \alpha_i), \tag{27d}$$

$$\Psi_{b_q} = p(b_q \mid \mathbf{r}_{\mathrm{LP}}, \mathbf{r}_{\mathrm{RP}}) = \mathcal{CN}\left(b_q; \mu_{b_q}, \eta_{b_q}\right). \tag{27e}$$

Specifically, Ψ_{b_q} and Ψ_{x_n} can be initialized using conventional approaches such as subsampling least squares (SLS) estimation [30] and linear minimum mean square error (LMMSE) detection [7]. Unlike the conventional assumption of uniform priors for $\mathbf{x}$, we adopt a non-uniform pseudo-prior derived from the LMMSE estimate, which serves as a more informative initialization. This approach, inspired by recent works [31], [32], has been shown to accelerate convergence and improve the numerical stability of iterative algorithms. Similar strategies are also referred to as non-uniform priors in [33].

B. Update rules

With a given factorization, the message passing algorithm can be interpreted as the exchange of two types of messages: the message from a factor node to a variable node, and the message from a variable node to a factor node.

In the considered model, each variable x_n is directly connected to both its local prior factor Ψ_{x_n} and the joint factor $\Psi_{\mathbf{s}}$. To simplify notation and avoid redundancy, we assume the messages exchanged along these edges are equivalent and omit repeated update steps in the sequel. Specifically, we have:

$$\begin{aligned} m_{x_n;\Psi_{x_n}} &= m_{\Psi_{\mathbf{s}};x_n}, \\ m_{x_n;\Psi_{\mathbf{s}}} &= m_{\Psi_{x_n};x_n}. \end{aligned} \tag{28}$$

Based on the above conventions, the message update steps can be outlined as follows.

1) : Update $m_{\Psi_{x_n};x_n} = \mathcal{CN}(x_n; \mu_{\Psi_{x_n};x_n}, \eta_{\Psi_{x_n};x_n})$.

To simplify the subsequent message passing, EP is used to approximate the categorical distribution with a complex Gaussian distribution [34]–[36]. With EP projection, the message is given by

$$m_{\Psi_{x_n};x_n}(x_n) \propto \frac{\mathrm{Proj}\left[\Psi_{x_n} m_{x_n;\Psi_{x_n}}\right]}{m_{x_n;\Psi_{x_n}}}. \tag{29}$$

2) : Update $m_{\Psi_{\mathbf{s}};\mathbf{s}} = \mathcal{CN}(\mathbf{s}; \boldsymbol{\mu}_{\Psi_{\mathbf{s}};\mathbf{s}}, \mathbf{C}_{\Psi_{\mathbf{s}};\mathbf{s}})$.

According to (27c), the information in the affine frequency domain is transformed into the time domain via the IDAFT. the message from node $\Psi_{\mathbf{s}}$ to node $\mathbf{s}$ can be derived as

$$\begin{aligned} \boldsymbol{\mu}_{\Psi_{\mathbf{s}};\mathbf{s}} &= \mathbf{A}^{\mathrm{H}} \boldsymbol{\mu}_{\mathbf{x};\Psi_{\mathbf{s}}}, \\ \mathbf{C}_{\Psi_{\mathbf{s}};\mathbf{s}} &= \mathbf{A}^{\mathrm{H}} \mathbf{C}_{\mathbf{x};\Psi_{\mathbf{s}}} \mathbf{A}, \end{aligned} \tag{30}$$

where $\boldsymbol{\mu}_{\mathbf{x};\Psi_{\mathbf{s}}}$ is defined by $\boldsymbol{\mu}_{\mathbf{x};\Psi_{\mathbf{s}}(n)} = \mu_{x_n;\Psi_{\mathbf{s}}}$, and $\mathbf{C}_{\mathbf{x};\Psi_{\mathbf{s}}}$ is a diagonal matrix with $\mathbf{C}_{\mathbf{x};\Psi_{\mathbf{s}}(n,n)} = \eta_{x_n;\Psi_{\mathbf{s}}}$.

3) : Update $m_{\mathbf{s};\Psi_{\mathbf{z}_q}} = \mathcal{CN}(\mathbf{z}_q; \boldsymbol{\mu}_{\Psi_{\mathbf{s}};\mathbf{z}_q}, \mathbf{C}_{\Psi_{\mathbf{s}};\mathbf{z}_q})$.

The message forward from node $\mathbf{s}$ to node $\Psi_{\mathbf{z}_q}$ can be expressed as

$$m_{\mathbf{s};\Psi_{\mathbf{z}_q}} \propto m_{\Psi_{\mathbf{s}};\mathbf{s}} \prod_{\tilde{q}\neq q} m_{\Psi_{\mathbf{z}_{\tilde{q}}};\mathbf{s}}. \tag{31}$$

According to the Gaussian multiplication lemma [34], we obtain

$$\begin{aligned}\mathbf{C}_{\mathbf{s};\Psi_{\mathbf{z}_q}} &= \left(\sum_{\tilde{q}\neq q} \mathbf{C}^{-1}_{\Psi_{\mathbf{z}_{\tilde{q}}};\mathbf{s}} + \mathbf{C}^{-1}_{\Psi_{\mathbf{s}};\mathbf{s}}\right)^{-1}, \\ \boldsymbol{\mu}_{\mathbf{s};\Psi_{\mathbf{z}_q}} &= \mathbf{C}_{\mathbf{s};\Psi_{\mathbf{z}_q}} \left(\sum_{\tilde{q}\neq q} \mathbf{C}^{-1}_{\mathbf{z}_{\tilde{q}};\mathbf{s}} \boldsymbol{\mu}_{\mathbf{z}_{\tilde{q}};\mathbf{s}} + \mathbf{C}^{-1}_{\Psi_{\mathbf{s}};\mathbf{s}} \boldsymbol{\mu}_{\Psi_{\mathbf{s}};\mathbf{s}}\right). \end{aligned} \tag{32}$$

The scalar form for the n-th element becomes:

$$\mu_{s_n;\Psi_{\mathbf{z}_q}} = \boldsymbol{\mu}_{\mathbf{s};\Psi_{\mathbf{z}_q(n)}}, \quad \eta_{s_n;\Psi_{\mathbf{z}_q}} = \mathbf{C}_{\mathbf{s};\Psi_{\mathbf{z}_q(n,n)}}. \tag{33}$$

4) : Update $m_{b_q;\Psi_{\mathbf{z}_{q(n)}}} = \mathcal{CN}(\mathbf{z}_{q(n)}; \mu_{b_q;\Psi_{\mathbf{z}_{q(n)}}}, \eta_{b_q;\Psi_{\mathbf{z}_{q(n)}}})$

The message can then be obtained by combining the contributions from all components except the n-th one, as follows:

$$\begin{aligned}\eta_{b_q;\Psi_{\mathbf{z}_{q(n)}}} &= \left(\sum_{\tilde{n}\neq n} 1/\eta_{\Psi_{\mathbf{z}_{q(\tilde{n})};b_q}} + 1/\eta_{b_q}\right)^{-1}, \\ \mu_{b_q;\Psi_{\mathbf{z}_{q(n)}}} &= \eta_{b_q;\Psi_{\mathbf{z}_{q(n)}}} \left(\sum_{\tilde{n}\neq n} \frac{\mu_{\Psi_{\mathbf{z}_{q(\tilde{n})};b_q}}}{\eta_{\Psi_{\mathbf{z}_{q(\tilde{n})};b_q}}} + \mu_{b_q}/\eta_{b_q}\right). \end{aligned} \tag{34}$$

5) : Update $m_{\Psi_{\mathbf{r}};\mathbf{z}_{q(n)}} = \mathcal{CN}(\mathbf{z}_{q(n)}; \mu_{\Psi_{\mathbf{r}};\mathbf{z}_{q(n)}}, \eta_{\Psi_{\mathbf{r}};\mathbf{z}_{q(n)}})$.

The update of $m_{\Psi_{\mathbf{r}};\mathbf{z}_q}$ can be interpreted as a soft interference cancellation process, where the residual interference-plus-noise component can be approximated as a complex Gaussian random variable according to the central limit theorem (CLT), as shown below:

$$\mathbf{z}_{q(n)} = \mathbf{r}_{\mathrm{D}(n)} \underbrace{- \sum_{\tilde{q}\neq q} \mathbf{z}_{\tilde{q}(n)} + \mathbf{n}_{\mathrm{D}(n)}}_{\text{Residual interference plus noise}}. \tag{35}$$

The mean and covariance of the message can be approximated by the following expressions:

$$\begin{aligned}\eta_{\Psi_{\mathbf{r}};\mathbf{z}_{q(n)}} &= \sigma_n^2 + \sum_{\tilde{q}\neq q} \eta_{\Psi_{\mathbf{z}};\mathbf{z}_{\tilde{q}(n)}}, \\ \mu_{\Psi_{\mathbf{r}};\mathbf{z}_{q(n)}} &= \mathbf{r}_{\mathrm{D}(n)} - \sum_{\tilde{q}\neq q} \mu_{\Psi_{\mathbf{z}};\mathbf{z}_{q(n)}}, \end{aligned} \tag{36}$$

where

$$\begin{aligned}\mu_{\Psi_{\mathbf{z}_q};\mathbf{z}_{q(n)}} &= \mu_{b_q;\Psi_{\mathbf{z}_{q(n)}}} \mathbf{H}_{q(n,\dot{n})} \mu_{s_{\dot{n}};\Psi_{\mathbf{z}_q}}, \\ \eta_{\Psi_{\mathbf{z}_q};\mathbf{z}_{q(n)}} &= \eta_{b_q;\Psi_{\mathbf{z}_{q(n)}}} \left|\mathbf{H}_{q(n,\dot{n})} \mu_{s_{\dot{n}};\Psi_{\mathbf{z}_q}}\right|^2 \\ &+ \left|\mu_{b_q;\Psi_{\mathbf{z}_{q(n)}}}\right|^2 \mathbf{H}_{q(n,\dot{n})} \eta_{s_{\dot{n}};\Psi_{\mathbf{z}_q}} \mathbf{H}^*_{q(n,\dot{n})} \\ &+ \eta_{b_q;\Psi_{\mathbf{z}_{q(n)}}} \mathbf{H}_{q(n,\dot{n})} \eta_{s_{\dot{n}};\Psi_{\mathbf{z}_q}} \mathbf{H}^*_{q(n,\dot{n})}, \end{aligned} \tag{37}$$

where $\mathbf{H}_{q(n,\dot{n})}$ denotes the nonzero entry in the n-th row of $\mathbf{H}_q$.

6) : Update $m_{\Psi_{\mathbf{z}_{q(n)};b_q}} = \mathcal{CN}(b_q; \mu_{\Psi_{\mathbf{z}_{q(n)};b_q}}, \eta_{\Psi_{\mathbf{z}_{q(n)};b_q}})$.

According to the message passing rule of EP, the message from $\mathbf{z}_q$ to b_q is

$$\begin{aligned}&m_{\Psi_{\mathbf{z}_q};b_q} \\ &\propto \frac{\mathrm{Proj}\left[\int \Psi_{\mathbf{z}_q} m_{\mathbf{z}_q;\Psi_{\mathbf{z}_q}}(\mathbf{z}_q) m_{\mathbf{s};\Psi_{\mathbf{z}_q}}(\mathbf{s}) m_{b_q;\Psi_{\mathbf{z}_q}}(b_q)\, d\mathbf{z}_q d\mathbf{s}\right]}{m_{\Psi_{b_q};\mathbf{z}_q}} \\ &= \frac{\mathrm{Proj}\left[\int m_{\Psi_{\mathbf{r}};\mathbf{z}_q}(b_q\mathbf{H}_q\mathbf{s}) m_{\mathbf{s};\Psi_{\mathbf{z}_q}}(\mathbf{s})\, m_{\Psi_{b_q};\mathbf{z}_q}(b_q) d\mathbf{s}\right]}{m_{\Psi_{b_q};\mathbf{z}_q}}. \end{aligned} \tag{38}$$

Considering that the integral in the above equation is difficult to solve in closed form, $m_{\mathbf{s};\Psi_{\mathbf{z}_q}}$ is approximated by a Dirac mixture density with K_s components to simplify the integral:

$$f(s_n) = \sum_{k_s=1}^{K_s} w_{k_s} \cdot \delta(s_n - s^{k_s}_{q,n}), \tag{39}$$

where w_{k_s} denotes the positive weights satisfying $\sum_{k_s=1}^{K_s} w_{k_s} = 1$ and $s^{k_s}_{q,n}$ is sampling position for the n-th element in vector $\mathbf{s}$. Such an approximation is widely used in nonlinear problems [37] and can be obtained via random sampling or deterministic methods like generalized fibonacci grids sampling [38].

Benefiting from the structured decomposition provided by the time-domain BEM, each row of the channel matrix $\mathbf{H}_q$ contains only a single nonzero element. This sparsity enables the reformulation of high-dimensional computations into scalar-wise operations, thereby avoiding high-dimensional sampling and significantly reducing computational complexity. Expressing $\mathbf{s}$ in scalar form and substituting (39) into (38), the approximated message can be written as:

$$\begin{aligned}&m_{\Psi_{\mathbf{z}_{q(n)};b_q}} \\ &\propto \frac{\mathrm{Proj}\left[m_{\Psi_{b_q};\mathbf{z}_{q(n)}} \sum_{k_s=1}^{K_s} w_{k_s} \mathcal{CN}\left(b_q; \mu^{k_s}_{q,n}, \eta^{k_s}_{q,n}\right) / |\mathbf{H}_{q(n,\dot{n})} s^{k_s}_{q,\dot{n}}|^2\right]}{m_{b_q;\Psi_{\mathbf{z}_{q(n)}}}} \\ &= \frac{\mathrm{Proj}\left[\sum_{k_s=1}^{K_s} P^{k_s}_{q,n} \mathcal{CN}(b_q; e^{k_s}_{q,n}, v^{k_s}_{q,n})\right]}{m_{b_q;\Psi_{\mathbf{z}_{q(n)}}}}. \end{aligned} \tag{40}$$

The integration over the Dirac mixture leads to a K_s-component Gaussian mixture inside the projection operator, as shown in (40), where $P^{k_s}_{q,n}$ denotes the normalized weight, and $\mathcal{CN}(b_q; e^{k_s}_{q,n}, v^{k_s}_{q,n})$ represents the corresponding complex Gaussian distribution:

$$\begin{aligned}P^{k_s}_{q,n} &\propto \frac{w_{k_s} \mathcal{CN}(0; \mu_{b_q;\Psi_{\mathbf{z}_{q(n)}}} - \mu^{k_s}_{q,n}, \eta_{b_q;\Psi_{\mathbf{z}_{q(n)}}} + \eta^{k_s}_{q,n})}{|\mathbf{H}_{q(n,\dot{n})} s^{k_s}_{q,n}|^2}, \\ v^{k_s}_{q,n} &= \left(1/\eta^{k_s}_{q,n} + 1/\eta_{b_q;\Psi_{\mathbf{z}_{q(n)}}}\right)^{-1}, \\ e^{k_s}_{q,n} &= v^{k_s}_{q,n} \left(\mu^{k_s}_{q,n}/\eta^{k_s}_{q,n} + \mu_{b_q;\Psi_{\mathbf{z}_{q(n)}}}/\eta_{b_q;\Psi_{\mathbf{z}_{q(n)}}}\right), \end{aligned} \tag{41}$$

where

$$\mu^{k_s}_{q,n} = \frac{\mu_{\Psi_{\mathbf{r}};\mathbf{z}_q(n)}}{\mathbf{H}_{q(n,\dot{n})} s^{k_s}_{q,\dot{n}}}, \eta^{k_s}_{q,n} = \frac{\eta_{\Psi_{\mathbf{r}};\mathbf{z}_{q(n)}}}{|\mathbf{H}_{q(n,\dot{n})} s^{k_s}_{q,\dot{n}}|^2}.$$

After applying the projection operation to the K_s-component Gaussian mixture, the resulting complex Gaussian distribution has the following mean and variance:

$$\begin{aligned} e_{q,n}^{b} &= \sum_{k_s} P_{q,n}^{k_s} e_{q,n}^{k_s}, \\ v_{q,n}^{b} &= \sum_{k_s} P_{q,n}^{k_s} (v_{q,n}^{k_s} + |e_{q,n}^{k_s}|^2) - |e_{q,n}^{b}|^2. \end{aligned} \tag{42}$$

By combining (40) and (42), the message $m_{\Psi_{\mathbf{z}_q(n)};b_q}$ can be updated as:

$$\begin{aligned} \eta_{\Psi_{\mathbf{z}_q(n)};b_q} &= \left(1/v_{q,n}^{b} - 1/\eta_{b_q;\Psi_{\mathbf{z}_q(n)}}\right)^{-1}, \\ \mu_{\Psi_{\mathbf{z}_q(n)};b_q} &= \eta_{\Psi_{\mathbf{z}_q(n)};b_q} \left(e_{q,n}^{s}/v_{q,n}^{b} - \mu_{b_q;\Psi_{\mathbf{z}_q(n)}}/\eta_{b_q;\Psi_{\mathbf{z}_q(n)}}\right). \end{aligned} \tag{43}$$

7) : Update $m_{\Psi_{\mathbf{z}_q};s_n} = \mathcal{CN}(s_n; \mu_{\Psi_{\mathbf{z}_q};s_n}, \eta_{\Psi_{\mathbf{z}_q};s_n})$.

Similar to the previous step, the Dirac mixture approximation is adopted to simplify integral computations. $m_{b_q;\Psi_{\mathbf{z}_q}}$ is approximated by a Dirac mixture density with K_b components:

$$f(b_q) = \sum_{k_b=1}^{K_b} w_{k_b} \cdot \delta(b_q - b_q^{k_b}). \tag{44}$$

The message approximated via sampling can be expressed as

$$\begin{aligned} & m_{\Psi_{\mathbf{z}_q};s_n} \\ \propto & \frac{\text{Proj}\left[m_{s_n;\Psi_{\mathbf{z}_q}} \sum_{k_b=1}^{K_b} w_{k_b} \mathcal{CN}\left(s_n; \mu_{q,n}^{k_b}, \eta_{q,n}^{k_b}\right)/|\mathbf{H}_{q(\ddot{n},n)} b_q^{k_b}|^2\right]}{m_{s_n;\Psi_{\mathbf{z}_q}}} \\ = & \frac{\text{Proj}\left[\sum_{k_b=1}^{K_b} P_{q,n}^{k_b} \mathcal{CN}\left(s_n; e_{q,n}^{k_b}, v_{q,n}^{k_b}\right)\right]}{m_{s_n;\Psi_{\mathbf{z}_q}}}. \end{aligned} \tag{45}$$

where $\mathbf{H}_{q(\ddot{n},n)}$ denotes the nonzero entry in the n-th column of $\mathbf{H}_q$.

The integration over the Dirac mixture leads to a K_b-component Gaussian mixture inside the projection operator, as shown in (45), where $P_{q,n}^{k_b}$ denotes the weight, and $\mathcal{CN}(s_n; e_{q,n}^{k_b}, v_{q,n}^{k_b})$ represents the corresponding complex Gaussian distribution:

$$\begin{aligned} P_{q,n}^{k_b} &\propto \frac{w_{k_b} \mathcal{CN}(0; \mu_{s_n;\Psi_{\mathbf{z}_q}} - \mu_{q,n}^{k_b}, \eta_{s_n;\Psi_{\mathbf{z}_q}} + \eta_{q,n}^{k_b})}{|\mathbf{H}_{q(\ddot{n},n)} b_q^{k_b}|^2}, \\ v_{q,n}^{k_b} &= (1/\eta_{s_n;\Psi_{\mathbf{z}_q}} + 1/\eta_{q,n}^{k_b})^{-1}, \\ e_{q,n}^{k_b} &= v_{q,n}^{k_b} (\mu_{s_n;\Psi_{\mathbf{z}_q}}/\eta_{s_n;\Psi_{\mathbf{z}_q}} + \mu_{q,n}^{k_b}/\eta_{q,n}^{k_b}), \end{aligned} \tag{46}$$

where

$$\mu_{q,n}^{k_b} = \frac{\mu_{\Psi_{\mathbf{r}};\mathbf{z}_q(\ddot{n})}}{\mathbf{H}_{q(\ddot{n},n)} b_q^{k_b}}, \eta_{q,n}^{k_b} = \frac{\eta_{\Psi_{\mathbf{r}};\mathbf{z}_q(\ddot{n})}}{|\mathbf{H}_{q(\ddot{n},n)} b_q^{k_b}|^2}.$$

Following the derivation in (42), $e_{q,n}^{s}$ and $v_{q,n}^{s}$ can be similarly obtained and are omitted here for brevity. The updated message $m_{\Psi_{\mathbf{z}_q};s_n}$ is given by:

$$\begin{aligned} \eta_{\Psi_{\mathbf{z}_q};s_n} &= \left(1/v_{q,n}^{s} - 1/\eta_{s_n;\Psi_{\mathbf{z}_q}}\right)^{-1}, \\ \mu_{\Psi_{\mathbf{z}_q};s_n} &= \eta_{\Psi_{\mathbf{z}_q};s_n} \left(e_{q,n}^{s}/v_{q,n}^{s} - \mu_{s_n;\Psi_{\mathbf{z}_q}}/\eta_{s_n;\Psi_{\mathbf{z}_q}}\right). \end{aligned} \tag{47}$$

8) : Update $m_{\mathbf{s};\Psi_{\mathbf{s}}} = \mathcal{CN}(\mathbf{s}; \boldsymbol{\mu}_{\mathbf{s};\Psi_{\mathbf{s}}}, \mathbf{C}_{\mathbf{s};\Psi_{\mathbf{s}}})$.

According to the Gaussian multiplication lemma, the message forward from node $\mathbf{s}$ to node $\Psi_{\mathbf{s}}$ can be updated as

$$\begin{aligned} \mathbf{C}_{\mathbf{s};\Psi_{\mathbf{s}}} &= \left(\sum_{q} \mathbf{C}_{\Psi_{\mathbf{z}_q};\mathbf{s}}^{-1}\right)^{-1}, \\ \boldsymbol{\mu}_{\mathbf{s};\Psi_{\mathbf{s}}} &= \mathbf{C}_{\mathbf{s};\Psi_{\mathbf{s}}} \left(\sum_{q} \mathbf{C}_{\Psi_{\mathbf{z}_q};\mathbf{s}}^{-1} \boldsymbol{\mu}_{\Psi_{\mathbf{z}_q};\mathbf{s}}\right). \end{aligned} \tag{48}$$

where $\boldsymbol{\mu}_{\Psi_{\mathbf{z}_q};\mathbf{s}}$ is defined by $\boldsymbol{\mu}_{\Psi_{\mathbf{z}_q};\mathbf{s}_{(n)}} = \mu_{\Psi_{\mathbf{z}_q};s_n}$, and $\mathbf{C}_{\Psi_{\mathbf{x}};\mathbf{x}}$ is a diagonal matrix with $\mathbf{C}_{\Psi_{\mathbf{z}_q};\mathbf{s}_{(n,n)}} = \eta_{\Psi_{\mathbf{z}_q};s_n}$.

9) : Update $m_{\Psi_{\mathbf{s}};x_n} = \mathcal{CN}(x_n; \mu_{\Psi_{\mathbf{s}};x_n}, \eta_{\Psi_{\mathbf{s}};x_n})$.

By transforming the message from the time domain back to the affine frequency domain, we obtain:

$$\begin{aligned} \mu_{\Psi_{\mathbf{s}};x_n} &= \left[\mathbf{A}\boldsymbol{\mu}_{\mathbf{s};\Psi_{\mathbf{s}}}\right]_{(n)}, \\ \eta_{\Psi_{\mathbf{s}};x_n} &= \left[\mathbf{A}\mathbf{C}_{\mathbf{s};\Psi_{\mathbf{s}}}\mathbf{A}^{\mathrm{H}}\right]_{(n,n)}. \end{aligned} \tag{49}$$

C. Inference

The desired estimates $\hat{b}_q$ and $\hat{x}_n$ can be obtained by computing the approximated posterior distribution, as follows:

$$\begin{aligned} \hat{x}_n &= \arg\max_{\alpha \in \mathcal{S}} \quad \Psi_{x_n}(x_n = \alpha)\ m_{x_n;\Psi_{x_n}}, \\ \hat{b}_q &= \left(\sum_{n} \frac{1}{\eta_{\Psi_{\mathbf{z}_q(n)};b_q}} + \frac{1}{\eta_{b_q}}\right)^{-1} \left(\sum_{n} \frac{\mu_{\Psi_{\mathbf{z}_q(n)};b_q}}{\eta_{\Psi_{\mathbf{z}_q(n)};b_q}} + \frac{\mu_{b_q}}{\eta_{b_q}}\right). \end{aligned} \tag{50}$$

By substituting the estimated result $\hat{b}_q$ in (50) into (24), the time-domain reconstruction matrix is obtained. Meanwhile, the estimate $\hat{x}_n$ is demapped onto the constellation to recover the transmitted bit.

D. Algorithm Description and Discussion

According to the aforementioned derivations, the SEP-based time domain JED algorithm proposed for AFDM systems is concluded in Algorithm 1.

To facilitate the convergence and stability of the proposed algorithm, two synergistic approaches are employed:

- A damping factor $g \in [0, 1]$ is introduced to regulate the convergence rate : $m_{\text{new}} = g \cdot m_{\text{new}} + (1 - g) \cdot m_{\text{old}}$;
- To address potential negative variances in EP iterations, clipping is applied to constrain the precision values $1/\eta$ (defined as the reciprocal of variance) within a numerically stable range, thereby ensuring numerical stability and preventing divergence;

E. Complexity Analysis

Based on Algorithm 1, the complexity analysis is presented in Table 1. Steps 3–5 involve repeated operations, which can be simplified using the identity $\sum_{n \neq \tilde{n}} f(n) = \sum_n f(n) - f(\tilde{n})$ and precomputing $\sum_n f(n)$. For instance, in Step 4, this optimization reduces the complexity from $\mathcal{O}(QN_{\text{D}}{}^2)$ to $\mathcal{O}(QN_{\text{D}})$. Steps 2 and 7 can be efficiently implemented using the DAFT, achieving a reduced complexity of $\mathcal{O}(N_{\text{D}} \log N_{\text{D}})$. Additionally, since the iteration only concerns the diagonal elements

Algorithm 1: The Proposed SEP-Based JED Algorithm

Initialization
repeat
  for $n = 0$ **to** $N_D - 1$ **do**
    Update $m_{\Psi_{x_n};x_n}$ based on (29);
    Update $m_{x_n;\Psi_{\mathbf{s}}}$ based on (28);
  Update $m_{\Psi_{\mathbf{s}};\mathbf{s}}$ based on (30);
  for $q = 1$ **to** Q **do**
    for $n = 0$ **to** $N_D - 1$ **do**
      Update $m_{s_n;\Psi_{\mathbf{z}_q}}$ based on (32-33);
      Update $m_{b_q;\Psi_{\mathbf{z}_{q(n)}}}$ based on (34);
      Update $m_{\Psi_{\mathbf{r}};\mathbf{z}_{q(n)}}$ based on (36-37);
      Update $m_{\Psi_{\mathbf{z}_{q(n)}};b_q}$ based on (39-43);
      Update $m_{\Psi_{\mathbf{z}_q};s_n}$ based on (44-47);
  Update $m_{\mathbf{s};\Psi_{\mathbf{s}}}$ based on (48);
  for $n = 0$ **to** $N_D - 1$ **do**
    Update $m_{\Psi_{\mathbf{s}};x_n}$ based on (49);
    Update $m_{x_n;\Psi_{x_n}}$ based on (28);
until *termination condition is met*;
Output: $\hat{b}_q$, $\forall q \in [1, Q]$; $\hat{x}_n$, $\forall n \in [0, N_{\mathrm{D}} - 1]$

TABLE I: Complexity analysis based on Algorithm 1.

Step	Complexity	Step	Complexity	Step	Complexity
1	$\mathcal{O}(MN)$	2	$\mathcal{O}(N \log N)$	3	$\mathcal{O}(QN)$
4	$\mathcal{O}(QN)$	5	$\mathcal{O}(QN)$	6	$\mathcal{O}(K_s QN)$
7	$\mathcal{O}(K_b QN)$	8	$\mathcal{O}(QN)$	9	$\mathcal{O}(N \log N)$

of the variance matrix, the output variances in these steps can be directly computed via averaging the input variances, eliminating the need for multiplication with the AFT matrix. Incorporating the above optimizations, the overall per-iteration complexity is approximately $\mathcal{O}(MN_{\mathrm{D}} + N_{\mathrm{D}} \log N_{\mathrm{D}} + (K_s + K_b)QN_{\mathrm{D}})$.

V. Simulation Results

In this section, we evaluate the performance of the proposed algorithm in terms of NMSE for channel estimation and BER for signal detection, to verify its effectiveness in JED.

A. Simulation Setup

The specific simulation parameters are as follows.

Channel setup: The number of propagation paths was set to $N_{\text{path}} = 20$, with a maximum delay tap of $l_{\max} = 4$. Each path follows an exponentially decaying power delay profile. The channel was modeled with integer-valued delay taps and fractional Doppler shifts, where the Doppler frequencies were uniformly distributed over the range $[-f_{\max}, f_{\max}]$.

Communication system setup: The transmitter is assumed to know the maximum delay for guard interval design, while the receiver is assumed to have perfect phase compensation and time synchronization. Unless otherwise specified, we consider an AFDM system operating at a carrier frequency of 9 GHz, with a subcarrier spacing of 15 kHz and a total of 512 subcarriers. In the following simulations, $\mathrm{SNR}_{\mathrm{P}}$ and $\mathrm{SNR}_{\mathrm{D}}$ denote the symbol energy-to-noise ratios for pilot and data signals, respectively.

TABLE II: Complexity comparison

(N_g: Number of Doppler grid points; T_{iter}: Iteration count; M: Constellation order; $P_{\mathrm{t}} = l_{\max} + 1$; $\beta_{\mathrm{t}} = 2l_{\max} + 1$.)

Algorithm	Channel Estimation	Detection
GS + LMMSE	$\mathcal{O}(N_g^{P_{\mathrm{t}}})$	$\mathcal{O}([P_{\mathrm{t}}^2 + \beta_{\mathrm{t}}^2 + \log(N_{\mathrm{D}})]N_{\mathrm{D}})$
SLS + LMMSE	$\mathcal{O}(QN_{\mathrm{P}})$	$\mathcal{O}([P_{\mathrm{t}}^2 + \beta_{\mathrm{t}}^2 + \log(N_{\mathrm{D}})]N_{\mathrm{D}})$
SEP	$\mathcal{O}(T_{\text{iter}}[MN_{\mathrm{D}} + N_{\mathrm{D}} \log N_{\mathrm{D}} + (K_s + K_b)QN_{\mathrm{D}}])$	
PBiGAMP	$\mathcal{O}(T_{\text{iter}} QN_{\mathrm{D}}^2)$	

Algorithm details: The proposed SEP algorithm employs a generalized Fibonacci grid sampling method [38]. For iterative algorithms involved in the evaluation, the maximum number of iterations was set to 25. In addition, the algorithm is considered to converge early if the following stopping criterion is satisfied over three consecutive iterations:

$$\frac{\left\|\hat{\mathbf{b}}^{(t+1)} - \hat{\mathbf{b}}^{(t+2)}\right\|_2}{\left\|\hat{\mathbf{b}}^{(t+1)}\right\|_2} + \frac{\left\|\hat{\mathbf{b}}^{(t)} - \hat{\mathbf{b}}^{(t+1)}\right\|_2}{\left\|\hat{\mathbf{b}}^{(t)}\right\|_2} < 1 \times 10^{-5}.$$

We consider several baseline algorithms to benchmark the proposed SEP algorithm within the JED framework. *Grid search* (GS) is a representative channel estimation algorithms based on affine-frequency-domain pilot embedding [5], and also serves as a performance reference for superposed pilot schemes [17] under successive interference cancellation conditions. *LMMSE* denotes the low-complexity detection algorithm proposed in [7]. *SLS* corresponds to a time-domain pilot arrangement scheme that reconstructs the channel via interpolation using pilots placed on both sides of the data block [30]. *PBiGAMP* is a state-of-the-art, low-complexity solver for parametric bilinear inference problems [25], and has been widely adopted in recent JED systems [20]. *Genie-aided* represents the performance bound when one side of the bilinear model (either the channel or the signal) is assumed to be perfectly known. Among the above algorithms, GS performs channel estimation based on the affine-frequency-domain pilot arrangement, while the others, including SEP, SLS, PBiGAMP, and Genie-aided, are built upon time-domain pilot arrangements.

The computational complexities of the proposed and baseline algorithms are summarized in Table II. PBiGAMP, as the state-of-the-art algorithm for JED, has a per-iteration complexity of $\mathcal{O}(QN_{\mathrm{D}}^2)$, which scales quadratically with the number of subcarriers N_{D}. Therefore, under the assumption of a large N_{D}, the proposed scheme achieves significantly lower computational complexity, exhibiting log-linear rather than quadratic scaling with respect to N_{D}.

B. Results and Discussion

Fig. 5 presents a comparative analysis of the proposed algorithm against several baseline schemes. The conventional GS+LMMSE and SLS+LMMSE methods, which do not incorporate joint processing, serve as representative non-JED baselines. In contrast, algorithms that perform JED exhibit markedly improved performance, approaching the genie-aided

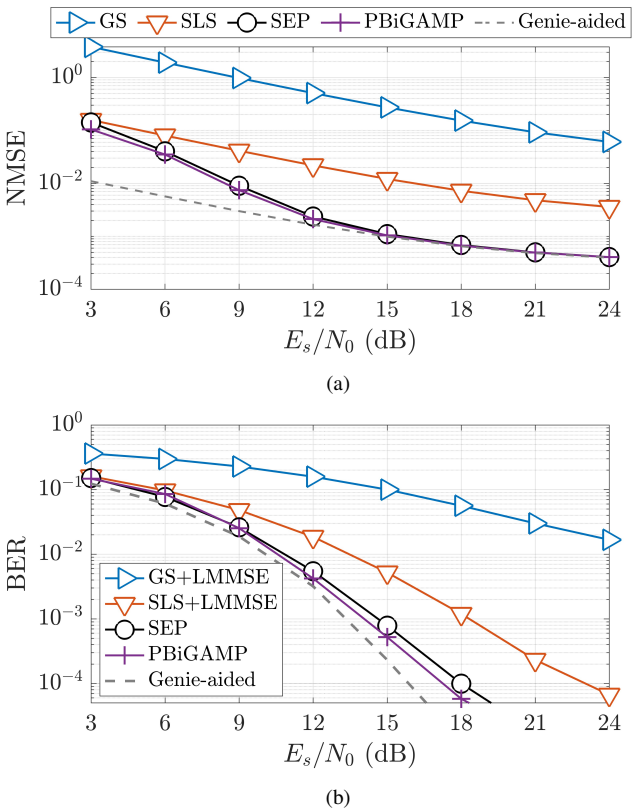

Fig. 5: Performance comparison of different algorithms versus SNR in terms of NMSE for channel estimation and BER for signal detection, with 4-QAM constellation, $\mathrm{SNR_P} = \mathrm{SNR_D}$, $k_v = 4$, $N_\mathrm{p} = 4l_\mathrm{max}$, and $K_s = K_b = 7$.

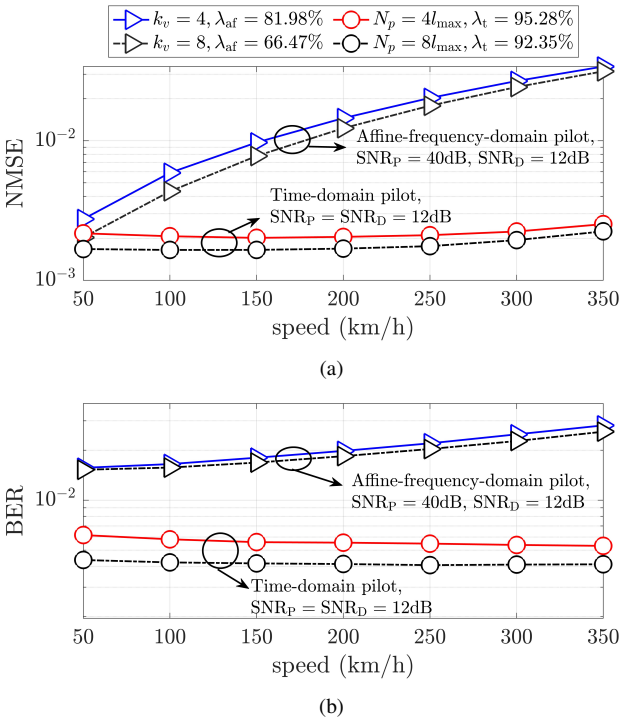

Fig. 6: Performance comparison of affine-frequency-domain and time-domain pilot arrangements under different user mobility conditions in terms of NMSE for channel estimation and BER for signal detection with 4-QAM constellation and $K_s = K_b = 7$.

bound. Specifically, at a target BER of 10^{-4}, the proposed algorithm achieves a performance gain of approximately 5 dB over the SLS baseline. Moreover, when $E_s/N_0 > 15$ dB, the corresponding channel estimation NMSE of the proposed method closely approaches the genie-aided lower bound. The PBiGAMP algorithm exhibits the best overall performance among the evaluated schemes, primarily due to the characteristics of the matrix $\mathbf{H}_q\mathbf{A}$ in (25), which align well with the algorithm's underlying assumptions of dense matrix and large system dimensions. However, the high matrix density also leads to substantial computational complexity, which may hinder its practical deployment in systems with limited processing resources. By contrast, the proposed SEP algorithm adopts scalar-level sampling approximations that significantly reduce computational burden while maintaining competitive performance. Although a marginal performance loss is observed compared to PBiGAMP, the substantial reduction in complexity makes SEP a more practical solution for AFDM systems with large subcarrier dimensions.

Fig. 6 compares the performance of the affine-frequency-domain pilot arrangement scheme (Algorithm: GS+LMMSE) and the time-domain pilot arrangement scheme (Algorithm: SEP) under varying user mobility speeds. Considering that subcarrier-based pilot embedding schemes benefit significantly from higher pilot SNR due to their susceptibility to interference, a higher $\mathrm{SNR_P}$ than $\mathrm{SNR_D}$ is allocated in this simulation to better reflect their performance under favorable conditions. As observed, both schemes exhibit similar performance at a low speed of 50 km/h. However, as the user speed increases, the performance of the affine-frequency-domain scheme degrades noticeably, whereas the time-domain scheme maintains consistently strong performance across all mobility levels, demonstrating superior adaptability to high-speed scenarios. The performance gap primarily arises from the fact that the affine-frequency-domain scheme relies on the assumption that each path can be well resolved under the affine-frequency-domain equivalent channel matrix. However, in scenarios with rich scattering, the limited path resolvability constrains the effectiveness of the grid search algorithm. From another perspective, the grid search essentially approximates the time-varying channel using a single Fourier basis, which leads to approximation errors that are less severe in low-mobility scenarios—hence the relatively better performance in such conditions. Moreover, the affine-frequency-domain scheme suffers from substantial transmission efficiency loss due to the insertion of numerous guard intervals. While increasing the guard length can mitigate pilot-data interference, the resulting performance improvement is limited. In contrast, the time-domain scheme not only achieves higher spectral efficiency but also offers superior JED performance, making it more suitable for high-mobility applications.

Fig. 7 presents the performance of the proposed algorithm

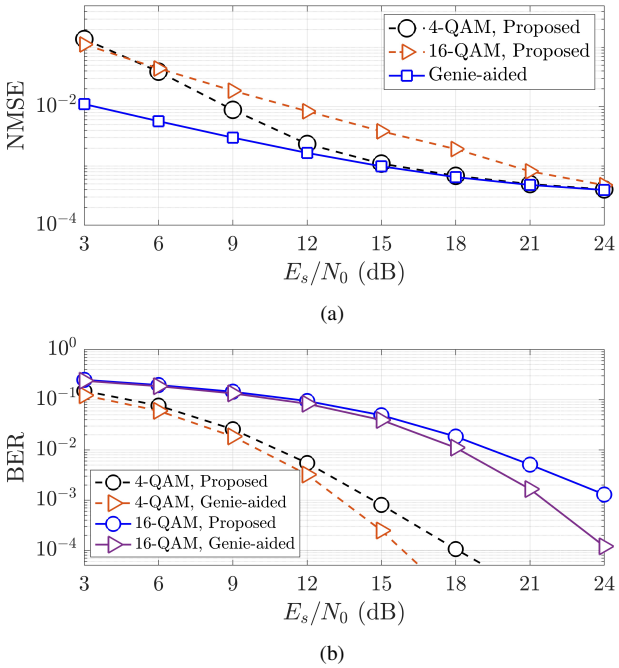

Fig. 7: Performance comparison of the proposed algorithm under different constellation orders in terms of NMSE for channel estimation and BER for signal detection, with $\mathrm{SNR_P} = \mathrm{SNR_D}$, $N_\mathrm{p} = 4l_{\max}$ (4-QAM), $N_\mathrm{p} = 8l_{\max}$ (16-QAM), and $K_s = K_b = 7$.

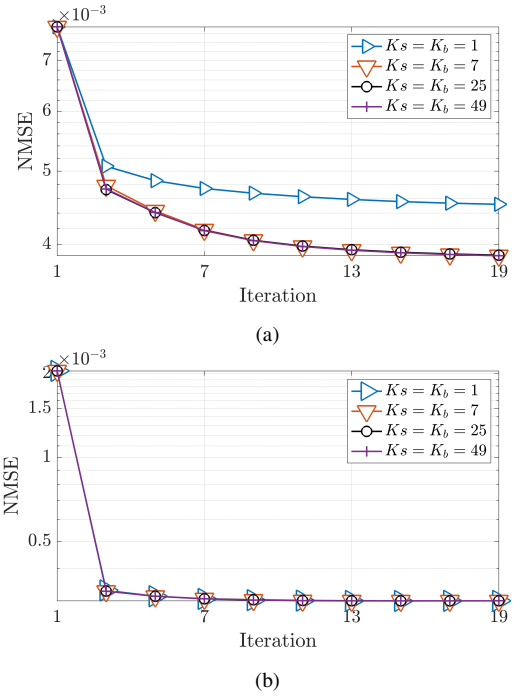

Fig. 8: Convergence behavior versus number of sampling points. (a): NMSE convergence at $\mathrm{SNR_P} = \mathrm{SNR_D} = 12$ dB; (b): NMSE convergence at $\mathrm{SNR_P} = \mathrm{SNR_D} = 20$ dB.

under 4-QAM and 16-QAM constellations. In terms of NMSE for channel estimation, 4-QAM exhibits slightly lower error than 16-QAM at 3 dB, owing to the longer pilot length used in the 16-QAM case. However, as the SNR increases, 4-QAM consistently outperforms 16-QAM in both NMSE and BER. This advantage is attributed to the larger minimum Euclidean distance of 4-QAM, which reduces symbol ambiguity and enhances the effectiveness of data-aided iterative estimation. In contrast, the denser 16-QAM constellation is more vulnerable to noise, introducing greater uncertainty in the JED message passing process. Notably, at high SNR (e.g., $E_s/N_0 > 21$ dB for 16-QAM), the NMSE of the proposed algorithm approaches the genie-aided bound. On the other hand, at low SNR, the BER performance of the proposed algorithm is closer to the genie-aided BER bound. This is because, in low-SNR regimes, additive noise dominates the overall error performance, whereas in high-SNR regimes, the residual interference caused by imperfect channel estimation becomes the primary limiting factor. Overall, 4-QAM demonstrates superior performance in both channel estimation and signal detection, making it a favorable choice in intermediate SNR regimes where reliability is critical. In contrast, 16-QAM requires higher SNR levels or the assistance of advanced techniques, such as channel coding or multiple-input multiple-output schemes, to achieve performance comparable to the robustness provided by 4-QAM.

Fig. 8 illustrates the convergence behavior of SEP-based channel estimation under different numbers of samples used to approximate the Gaussian distribution. When $k_s = k_b = 1$, the Dirac mixture reduces to a Dirac-delta function, ignoring the variance in the message passing process [39]. When $k_s = k_b > 1$, the approximation corresponds to a deterministic sampling scheme (e.g., eneralized fibonacci grids sampling). As shown, under low SNR conditions, the Dirac mixture yields better performance than a single Dirac-delta approximation. For example, the NMSE improves from 0.0045 to 0.0038, with a relative gain of approximately 15.6%. Moreover, even with a small number of sampling points, the Dirac mixture achieves excellent performance, and further increasing the number of samples does not result in noticeable improvements. In contrast, at high SNR, the performance of the single Dirac-delta approximation becomes comparable to that of the Dirac mixture. This is because, according to the asymptotic property $\lim_{\eta\to 0}\mathcal{CN}(x;\mu,\eta) = \delta(x-\mu)$, the Dirac mixture approximation effectively reduces to a single Dirac-delta function $\delta(x-\mu)$ when the variances become sufficiently small, which commonly occurs in high-SNR regimes. This simplification also opens up the possibility of incorporating adaptive decision mechanisms to further reduce complexity. Due to space limitations, this direction is left for future work.

VI. Conclusion

In this paper, we proposed an AFDM transmission framework based on a novel time-domain pilot placement strategy. By introducing the notion of transmission efficiency, we highlighted the advantages of the proposed scheme over conventional affine-frequency-domain pilot designs. To enable efficient joint estimation and detection, we further formulated a bilinear inference problem in the time domain using a BEM. Building on this model, we developed a SEP algorithm

by leveraging EP message passing and Dirac mixture approximations. Simulation results confirmed that the proposed method achieves a favorable trade-off between performance and computational complexity.

Future work includes extending the proposed framework to doubly fractional-selective channels, where both delay and Doppler taps are fractional. We also plan to investigate the integration of channel coding to improve performance in low and moderate SNR regions, and to explore the potential of combining with Turbo structures.

REFERENCES

[1] H. Miao, J. Zhang, P. Tang, J. Meng, Q. Zhen, X. Liu, E. Liu, P. Liu, L. Tian, and G. Liu, "A survey of new mid-band/FR3 for 6G: Channel measurement, characterization and modeling in outdoor environment," *arXiv preprint arXiv:2504.06727*, 2025.

[2] C.-X. Wang, X. You, X. Gao, X. Zhu, Z. Li, C. Zhang, H. Wang, Y. Huang, Y. Chen, H. Haas, J. S. Thompson, E. G. Larsson, M. D. Renzo, W. Tong, P. Zhu, X. Shen, H. V. Poor, and L. Hanzo, "On the road to 6G: Visions, requirements, key technologies, and testbeds," *IEEE Commun. Surv. Tutorials*, vol. 25, no. 2, pp. 905–974, 2023.

[3] H. Hou, Y. Wang, X. Yi, W. Wang, and S. Jin, "Joint beam alignment and Doppler estimation for fast time-varying wideband mmWave channels," *IEEE Trans. Wireless Commun.*, vol. 23, no. 9, pp. 10 895–10 910, 2024.

[4] R. Hadani, S. Rakib, M. Tsatsanis, A. Monk, A. J. Goldsmith, A. F. Molisch, and R. Calderbank, "Orthogonal time frequency space modulation," in *2017 IEEE Wireless Communications and Networking Conference (WCNC)*, 2017, pp. 1–6.

[5] A. Bemani, N. Ksairi, and M. Kountouris, "Affine frequency division multiplexing for next generation wireless communications," *IEEE Trans. Wireless Commun.*, vol. 22, no. 11, pp. 8214–8229, 2023.

[6] W. Benzine, A. Bemani, N. Ksairi, and D. Slock, "Affine frequency division multiplexing for communications on sparse time-varying channels," in *GLOBECOM 2023 - 2023 IEEE Global Communications Conference*, 2023, pp. 4921–4926.

[7] Z. Li, C. Zhang, G. Song, X. Fang, X. Sha, and D. Slock, "Chirp parameter selection for affine frequency division multiplexing with MMSE equalization," *IEEE Trans. Commun.*, pp. 1–1, 2024.

[8] G. Liu, T. Mao, Z. Xiao, M. Wen, R. Liu, J. Zhao, E. Basar, Z. Wang, and S. Chen, "Pre-chirp-domain index modulation for full-diversity affine frequency division multiplexing towards 6G," *IEEE Trans. Wireless Commun.*, pp. 1–1, 2025.

[9] H. Yuan, Y. Xu, X. Guo, Y. Ge, T. Ma, H. Li, D. He, and W. Zhang, "PAPR reduction with pre-chirp selection for affine frequency division multiplexing," *IEEE Wireless Commun. Lett.*, vol. 14, no. 3, pp. 736–740, 2025.

[10] Z. Li, L. Ou, C. Zhang, X. Fang, and X. Sha, "A hybrid carrier communication system based on weighted affine fourier transform," *IEEE Commun. Lett.*, vol. 28, no. 7, pp. 1629–1633, 2024.

[11] Q. Luo, P. Xiao, Z. Liu, Z. Wan, N. Thomos, Z. Gao, and Z. He, "AFDM-SCMA: A promising waveform for massive connectivity over high mobility channels," *IEEE Trans. Wireless Commun.*, vol. 23, no. 10, pp. 14 421–14 436, 2024.

[12] J. Zhu, Y. Tang, F. Liu, X. Zhang, H. Yin, and Y. Zhou, "AFDM-based bistatic integrated sensing and communication in static scatterer environments," *IEEE Wireless Commun. Lett.*, vol. 13, no. 8, pp. 2245–2249, 2024.

[13] Y. Ni, P. Yuan, Q. Huang, F. Liu, and Z. Wang, "An integrated sensing and communications system based on affine frequency division multiplexing," *IEEE Trans. Wireless Commun.*, pp. 1–1, 2025.

[14] Djuro Stojanović, Igor Djurović, and Branimir R Vojcic. "Multicarrier communications based on the affine Fourier transform in doubly-dispersive channels," *EURASIP J. Wireless Commun. Networking*, pp. 1–10, 2010.

[15] H. Yin and Y. Tang, "Pilot aided channel estimation for AFDM in doubly dispersive channels," in *2022 IEEE/CIC International Conference on Communications in China (ICCC)*. IEEE, 2022, pp. 308–313.

[16] A. Bemani, N. Ksairi, and M. Kountouris, "Low complexity equalization for AFDM in doubly dispersive channels," in *ICASSP 2022-2022 IEEE International Conference on Acoustics, Speech and Signal Processing (ICASSP)*. IEEE, 2022, pp. 5273–5277.

[17] K. Zheng, M. Wen, T. Mao, L. Xiao, and Z. Wang, "Channel estimation for AFDM with superimposed pilots," *IEEE Trans. Veh. Technol.*, vol. 74, no. 2, pp. 3389–3394, 2025.

[18] Y. Liu, Y. L. Guan, and D. González, "Near-optimal BEM OTFS receiver with low pilot overhead for high-mobility communications," *IEEE Trans. Commun.*, vol. 70, no. 5, pp. 3392–3406, 2022.

[19] Y. Xiang, K. Xu, B. Xia, and X. Cheng, "Bayesian joint channel-and-data estimation for quantized OFDM over doubly selective channels," *IEEE Trans. Wireless Commun.*, vol. 22, no. 3, pp. 1523–1536, 2022.

[20] Y. Ma, N. Wu, J. A. Zhang, B. Li, and L. Hanzo, "Parametric bilinear iterative generalized approximate message passing reception of FTN multi-carrier signaling," *IEEE Trans. Commun.*, vol. 69, no. 12, pp. 8443–8458, 2021.

[21] X. Wang, W. Shen, C. Xing, J. An, and L. Hanzo, "Joint bayesian channel estimation and data detection for OTFS systems in LEO satellite communications," *IEEE Trans. Commun.*, vol. 70, no. 7, pp. 4386–4399, 2022.

[22] K. Ito, T. Takahashi, K. Furuta, S. Ibi, and G. T. F. De Abreu, "Joint channel and data estimation via parametric bilinear inference for OTFS demodulation," *IEEE Open J. Commun. Soc.*, 2024.

[23] K. R. R. Ranasinghe, H. S. Rou, G. T. F. De Abreu, T. Takahashi, and K. Ito, "Joint channel, data and radar parameter estimation for AFDM systems in doubly-dispersive channels," *IEEE Trans. Wireless Commun.*, 2024.

[24] N. K. Jha, H. Guo, and V. K. Lau, "Bayesian deep end-to-end learning for MIMO-OFDM system with delay-domain sparse precoder," *arXiv preprint arXiv:2504.20777*, 2025.

[25] J. T. Parker and P. Schniter, "Parametric bilinear generalized approximate message passing," *IEEE J. Sel. Top. Signal Process.*, vol. 10, no. 4, pp. 795–808, 2016.

[26] K. Furuta, T. Takahashi, K. Ito, and S. Ibi, "Joint channel and data estimation via bayesian parametric bilinear inference for OTFS transmission," in *2024 IEEE 21st Consumer Communications & Networking Conference (CCNC)*. IEEE, 2024, pp. 887–892.

[27] H. Qu, G. Liu, L. Zhang, M. A. Imran, and S. Wen, "Low-dimensional subspace estimation of continuous-doppler-spread channel in OTFS systems," *IEEE Trans. Commun.*, vol. 69, no. 7, pp. 4717–4731, 2021.

[28] T. Zemen and C. Mecklenbrauker, "Time-variant channel estimation using discrete prolate spheroidal sequences," *IEEE Trans. Signal Process.*, vol. 53, no. 9, pp. 3597–3607, 2005.

[29] S. Coleri, M. Ergen, A. Puri, and A. Bahai, "Channel estimation techniques based on pilot arrangement in OFDM systems," *IEEE Trans. Broadcast.*, vol. 48, no. 3, pp. 223–229, 2002.

[30] H. Qu, G. Liu, Y. Wang, Q. Chen, C. Yi, and J. Peng, "A time-domain approach to channel estimation and equalization for the SC-FDM system," *IEEE Trans. Broadcast.*, vol. 65, no. 4, pp. 713–726, 2019.

[31] J. Goldberger and A. Leshem, "Pseudo prior belief propagation for densely connected discrete graphs," in *2010 IEEE Information Theory Workshop on Information Theory (ITW 2010, Cairo)*, 2010, pp. 1–5.

[32] W. Zhou, Y. Shen, L. Li, Y. Huang, C. Zhang, and X. You, "Belief-selective propagation detection for MIMO systems," *IEEE Trans. Commun.*, vol. 71, no. 12, pp. 7244–7257, 2023.

[33] I. Santos, J. J. Murillo-Fuentes, E. Arias-de Reyna, and P. M. Olmos, "Turbo EP-based equalization: A filter-type implementation," *IEEE Trans. Commun.*, vol. 66, no. 9, pp. 4259–4270, 2018.

[34] A. Karataev, C. Forsch, and L. Cottatellucci, "Bilinear expectation propagation for distributed semi-blind joint channel estimation and data detection in cell-free massive MIMO," *IEEE Open J. Signal Process.*, vol. 5, pp. 284–293, 2024.

[35] Z. Zhao and D. Slock, "Expectation propagation based analysis of semi-blind channel estimation in cell-free systems," in *2024 IEEE 25th International Workshop on Signal Processing Advances in Wireless Communications (SPAWC)*, 2024, pp. 836–840.

[36] Z. Zhao and D. Slock, "Hierarchical expectation propagation for semi-blind channel estimation in cell-free networks," in *ICASSP 2025 - 2025 IEEE International Conference on Acoustics, Speech and Signal Processing (ICASSP)*, 2025, pp. 1–5.

[37] J. Steinbring and U. D. Hanebeck, "S2KF: The smart sampling Kalman filter," in *Proceedings of the 16th International Conference on Information Fusion*, 2013, pp. 2089–2096.

[38] D. Frisch and U. D. Hanebeck, "Deterministic gaussian sampling with generalized fibonacci grids," in *2021 IEEE 24th International Conference on Information Fusion (FUSION)*, 2021, pp. 1–8.

[39] F. Li, Z. Xu, and S. Zhu, "Variational-inference-based data detection for OFDM systems with imperfect channel estimation," *IEEE Trans. Veh. Technol*, vol. 62, no. 3, pp. 1394–1399, 2013.